Role of the Cr Buffer Layer in the Thickness-Dependent Ultrafast Magnetization Dynamics of $Co_2Fe_{0.4}Mn_{0.6}Si$ Heusler Alloy Thin Films

Santanu Pan,[1] Takeshi Seki,[2,3,4] Koki Takanashi,[2,3] and Anjan Barman[1,*]

[1]*Department of Condensed Matter Physics and Material Sciences, S. N. Bose National Centre for Basic Sciences, Block JD, Sector III, Salt Lake, Kolkata 700 106, India*

[2]*Institute for Materials Research, Tohoku University, Sendai 980-8577, Japan*

[3]*Center for Spintronics Research Network, Tohoku University, Sendai 980-8577, Japan*

[4]*JST PRESTO, Saitama 332-0012, Japan*

(Received 20 February 2017; revised manuscript received 2 May 2017; published 12 June 2017)

The epitaxial growth of the $Co_2Fe_{0.4}Mn_{0.6}Si$ (CFMS) Heusler alloy on MgO with high crystal orientation requires the use of a buffer layer. The utilization of the Cr buffer layer in a controlled manner without hampering the intrinsic CFMS properties remains a challenge. Here, we epitaxially grow the CFMS films on a Cr-buffered MgO substrate and investigate the thickness (t)-dependent variation in structural ordering, and its impact on magnetic Gilbert damping and magnetic anisotropy. We observe a regular improvement in the crystal structure with increasing t, which causes a similar increasing trend in saturation magnetization and magnetocrystalline anisotropy. Interestingly, we achieve a very low t-independent value of Gilbert damping parameter (α) of ~0.0045 because of an unaltered atomic-site ordering which indicates a different origin of magnetocrystalline anisotropy and α in this system. Notably, α also remains nearly independent of frequency (f) for a lower thickness regime in these CFMS films. The observation of a t-independent and f-independent value of α strongly suggests the suitability of a thinner CFMS film for device applications in the broadband frequency regime.

DOI: 10.1103/PhysRevApplied.7.064012

I. INTRODUCTION

Half-metallic ferromagnetic materials with a high degree of spin polarization and a low magnetic damping are of utmost importance for applications in spintronic devices such as low-energy-operated magnetic random access memory (MRAM) [1–3], a pure spin current emitter in the ferromagnetic-semiconductor heterojunction, etc. Recent theoretical research reveals that a cobalt- (Co) based full Heusler alloy, one kind of half-metal, comprises only one spin sub-band in the density of states at the Fermi level (E_F), while a finite energy gap exists in the other [4–6]. Because of a lower density of states at E_F, the spin-flip scattering gets suppressed significantly, leading to very low magnetic Gilbert damping [7], and high spin polarization. Theoretical study [8] as well as experimental investigations [9–14] show that Co_2MnSi (CMS) is one of the full Heusler alloys having high Curie temperature (~930 K) and very low Gilbert damping. Later, under rigid band assumption, it is found that the substitution of a fraction of Mn atoms with Fe atoms in CMS, i.e., $Co_2Fe_{0.4}Mn_{0.6}Si$ (CFMS) possesses a more stable spin-polarized band structure [15]. CFMS exhibits a higher Curie temperature (~1000 K) and a low value of the Gilbert damping parameter (α) [16,17]. In preceding experiments [16,18], the CFMS was deposited on MgO (001) or GaAs (001) substrates for investigation. However, an inevitable lattice-mismatch-induced strain (~5.1%) develops in CFMS directly deposited on MgO (001) [19]. Recently, our study [18] showed that structural ordering as well as static and dynamic magnetic properties strongly depend on the thickness of the CFMS thin film in the presence of strain and strain-induced defects due to the lattice mismatch. It is known that the lattice mismatch reduces to about 1.8% when CFMS is deposited on Cr instead of MgO [19]. Thus, several previous experiments [12,16,17,20,21] used buffer layers (such as Cr, Ag) to reduce the strain effect, and achieved a better control on the structural ordering. Further, improvements of magnetic properties with annealing temperature [22–24] and chemical composition [17,25] have also been investigated. However, it has been shown that the diffusion of the buffer layer atom may adversely affect the pristine properties of CFMS, which is undesirable [19,24,26–28]. So, the explicit role of the buffer layer on thickness-dependent strain relaxation, and the means to control the structural ordering, Gilbert damping parameter, and magnetocrystalline anisotropy with thickness remained ambiguous for a film in the absence of strain.

II. EXPERIMENTAL DETAILS

Thin films of CFMS with different thicknesses (t) are deposited on top of 20-nm-thick Cr layers. This bilayer

*Corresponding author.
abarman@bose.res.in

stack is grown on a single crystalline MgO (100) substrate using an ultrahigh vacuum magnetron sputtering system. The Cr layer is deposited at room temperature (RT) and subsequently annealed at 600 °C. On the Cr layer, the CFMS layer is deposited at RT followed by an *in situ* annealing process at 500 °C for 1 h. An additional 5-nm-thick cover layer of aluminum oxide (Al-O) is added on top of CFMS at RT to protect it from oxidation, and external degradation. Here, Cr is used as a buffer to promote the growth of CFMS on MgO. The values of t are chosen to be 10 nm ($B10$), 20 nm ($B20$), and 30 nm ($B30$). To investigate the surface structural quality, we have taken *in situ* reflection high-energy electron diffraction (RHEED) images during the deposition process. *Ex situ* x-ray diffraction (XRD) measurement is performed to determine the crystalline phase and degree of atomic-site ordering in the films. M-H loops at RT are measured using a vibrating sample magnetometer with an in-plane magnetic field applied along CFMS [110]. Precessional magnetization dynamics are measured using a time-resolved magneto-optical Kerr effect (TRMOKE) magnetometer, a two-color pump-probe experiment in noncollinear geometry [29]. The fundamental output from an amplifier laser system with a pulse width of ~40 fs (Libra, Coherent) is used as a probe and the second harmonic signal of the fundamental output is used as a pump. The use of different pump ($\lambda = 400$ nm, $\sigma_t \approx 50$ fs) and probe ($\lambda = 800$ nm, $\sigma_t \approx 40$ fs) wavelengths rules out the possibility of a dichroic bleaching artifact in the results. The probe beam is focused onto an area of ~100 μm^2 while the spot area is ~400 μm^2 for the pump beam on the sample surface. The samples are subjected to an in-plane external variable bias magnetic field (H).

III. RESULTS AND DISCUSSIONS

A. Structural properties

Figure 1(a) shows the XRD patterns measured in $\theta - 2\theta$ geometry at room temperature for Cr-buffered CFMS thin films with three different values of t. We have identified CFMS (200) and CFMS (400) peaks in addition to MgO (200) and Cr (200) peaks in the diffraction patterns. The presence of a (200) peak with sufficient intensity counts in our CFMS films signifies the formation of the $B2$ phase (the random position of Fe, Mn, and Si with respect to the Co position) or the $L2_1$ phase (completely ordered atomic positions of all atoms). The inset shows the variation in $I(400)$ and $I(200)/I(400)$, the integrated intensity ratio of the (200) and (400) peaks representing Co atomic-site ordering, with t. In our earlier study [18], we found a strong thickness dependence of the atomic-site ordering in CFMS thin films deposited on MgO without any buffer layer. Here, we observe a monotonically increasing $I(400)$, associated with the improvement in the cubic crystal structure with t. However, despite of the changes in the overall crystal structure, we achieved a thickness independent value of $I(200)/I(400)$ representing stable Co atomic-site ordering. This result suggests that in the case of strain-eliminated growth in the presence of a buffer layer, microscopic or atomic-site ordering is not affected significantly by the thickness of the CFMS thin film. In addition, Fig. 1(b) shows the in-plane XRD scan for (111) and (220) peaks which confirms the perfect epitaxial growth of the films. The presence of the (111) peak clearly proves the existence of the $L2_1$ phase in the 30-nm-thick

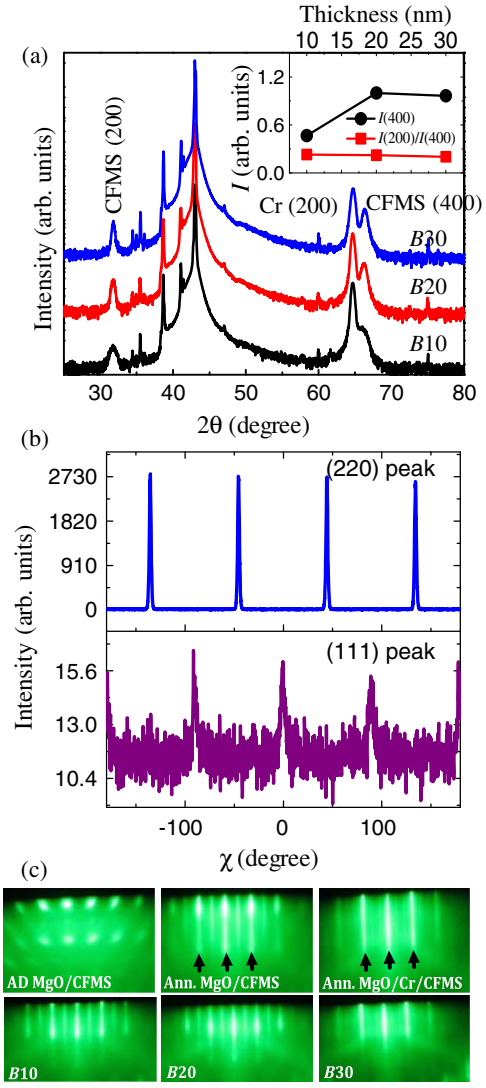

FIG. 1. (a) XRD patterns in conventional $\theta - 2\theta$ geometry for CFMS films with different values of thickness. The inset shows the evolution of integrated intensity $I(400)$ and the intensity ratio $I(200)/I(400)$ as a function of thickness for CFMS films. (b) In-plane XRD patterns for 30-nm-thick Cr-buffered CFMS films. Two panels show the intensity variation for two different peaks (111) and (220). (c) RHEED patterns for different CFMS films taken along MgO [100]. The first row shows as-deposited (AD) CFMS, annealed (Ann.) CFMS at 500°C and annealed CFMS on the Cr buffer layer with a CFMS layer thickness of 30 nm. The second row represents different CFMS thicknesses in Cr/CFMS films.

CFMS sample with a complete ordering of the atomic positions as opposed to the unbuffered CFMS thin films [18].

To investigate the layer growth during the deposition of CFMS, *in situ* RHEED images have been taken along the MgO [100] direction. The first row in Fig. 1(c) shows the RHEED images for 30-nm-thick as-deposited CFMS film on MgO, annealed CFMS film deposited on MgO, and annealed CFMS film deposited on Cr. One can clearly see that the spotty diffraction pattern in the as-deposited CFMS turns into long streak patterns after annealing, which indicates the epitaxial growth with crystal orientation MgO (001)‖CFMS (001), MgO [100]‖CFMS [110]. This tells us the horizontal and vertical growth directions of CFMS on MgO. CFMS (001) planes grow parallel to the MgO (001) planes, and the CFMS [110] direction, which is perpendicular to the CFMS (110) planes, is parallel to the MgO [100] direction. This tells us that the edge of the cubic crystal of the CFMS is oriented along 45° to the edge of the MgO cubic crystal structure. The symmetric streak lines become sharper after the addition of the Cr layer, which indicates the proper two-dimensional growth and flat surface due to the lattice matching between Cr and MgO. The second row in Fig. 1(c) represents the RHEED images for annealed CFMS films on the Cr buffer with varying t. We observe the similar RHEED patterns for all of the samples with buffer layers, which ensure no significant change in the development of the films with the variation in thickness.

B. Magnetic properties

Figure 2(a) shows the M-H loops measured at room temperature for $B10$, $B20$, and $B30$ with an external magnetic field applied along the CFMS [110] direction. We obtain the nearly square hysteresis loops with full remanence for all of the samples. The extracted values of saturation magnetization (M_S) and coercivity (H_C) are 860, 920, 930 emu/cm^3 and 22, 14, 13 Oe for $B10$, $B20$, $B30$, respectively, which are shown in Fig. 2(b). The substantial increment in M_S with an increasing t is attributable to the improvement in the cubic crystal structure. On the same ground, a similar monotonically decreasing trend in H_C is observed, which is consistent with a previous report [30]. The estimated M_S values for CFMS deposited on Cr are higher than the CFMS deposited on MgO [18]. This strongly implies the promotion of the crystal ordering and two-dimensional growth because of better lattice matching between CFMS and Cr. However, a slightly higher value of H_C is found, despite having strain eliminated growth, for CFMS on Cr. During the high-temperature annealing process, Cr can easily diffuse inside the CFMS layer [24,27], and hence, the presence of a few foreign Cr atoms inside CFMS, and Co-Cr disorder [26,28] are probably causing this enhancement in coercivity. It concludes that the deposition of CFMS on Cr promotes the crystal ordering without affecting the microscopic (chemical) ordering, even with a minor diffusion of Cr inside CFMS.

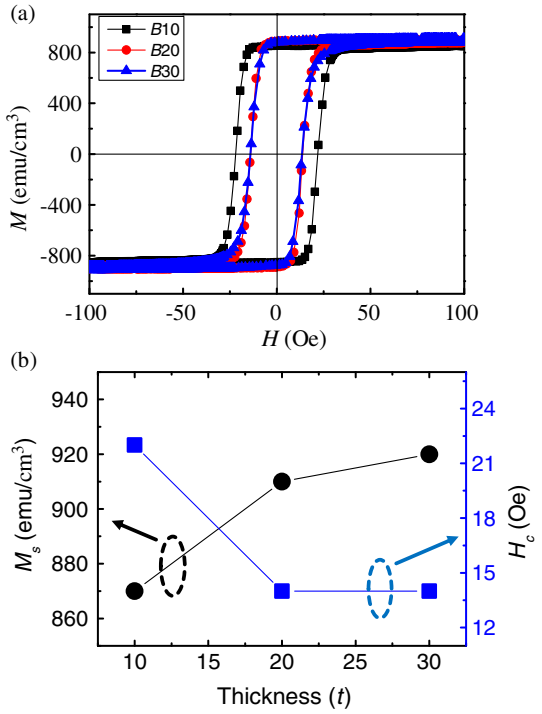

FIG. 2. (a) M-H loops for three different thickness values of CFMS films measured at room temperature. (b) Variation in M_S and H_C as a function of thickness.

The time-resolved Kerr rotation data obtained from the TRMOKE experiment can be divided into three distinct temporal regimes [29]. We observe an ultrafast demagnetization within ~400 fs and a fast relaxation within ~1.5 ps for all of the present CFMS samples. A biexponential background is subtracted from the data to extract the damped oscillatory component corresponding to the magnetization precession, and the power spectrum of the signal in the frequency domain is obtained by using the fast Fourier transform (FFT) algorithm. We analyzed all of the precessional Kerr rotation data corresponding to magnetization dynamics to extract the precession frequency (f), magnetocrystalline anisotropy, and Gilbert damping coefficient (α).

Figure 3(a) presents the measured Kerr rotation oscillations at a different strength of H for the CFMS film of thickness 30 nm. All of the measured data represent single-frequency (f) precession for the CFMS films. We have employed the macrospin modeling to analyze the time-dependent uniform precessional dynamics by solving the Landau-Lifshitz-Gilbert equation

$$\frac{d\hat{m}}{dt} = -\gamma(\hat{m} \times \vec{H}_{\text{eff}}) + \alpha\left(\hat{m} \times \frac{d\hat{m}}{dt}\right), \qquad (1)$$

where γ is the gyromagnetic ratio, and is related to the Landé g factor by $\gamma = (g\mu_B/\hbar)$, μ_B is the Bohr magneton,

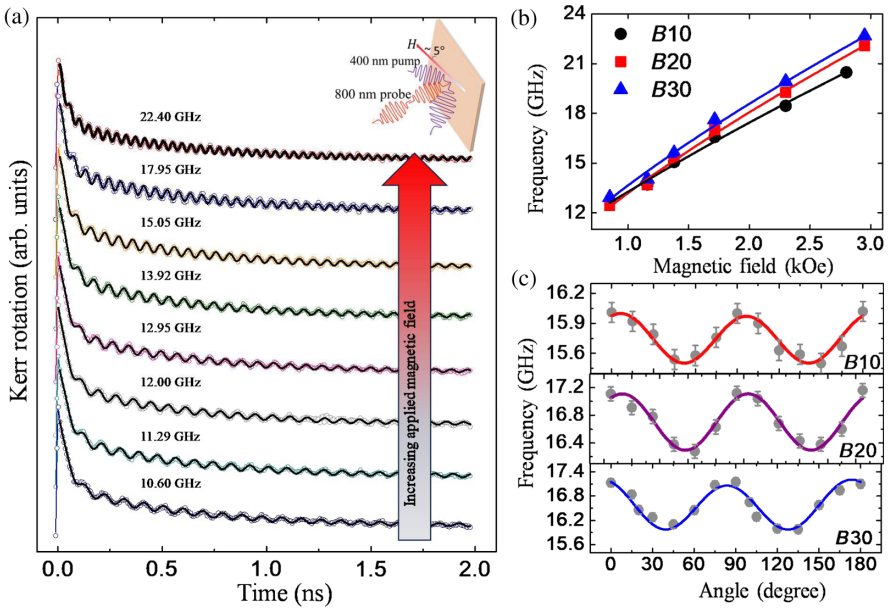

FIG. 3. (a) Time-dependent Kerr rotation data (scattered points) at different H values for the sample $B20$ and their best fits using Eq. (5) (solid lines). The inset shows the measurement configuration. (b) Variation in magnetization precession frequency (f) as a function of magnetic field, H (scattered points) fitted with Eq. (3) (solid line). (c) Evolution of f as a function of azimuthal angle φ with respect to the direction of H (scattered points) and their best fit using Eq. (2) (solid line).

and $\hbar$ is the reduced Planck's constant. H_{eff} is the total effective magnetic field consisting of the bias magnetic field (H_{bias}), exchange field (H_{ex}), dipolar field (H_{dip}), and anisotropy field (H_k), and α is the Gilbert damping coefficient as mentioned before. The solution to the linearized Landau-Lifshitz-Gilbert equation under small angle approximation including twofold and fourfold magnetocrystalline anisotropies in the effective magnetic field leads to the relation between f and H as follows:

$$f = \frac{\gamma}{2\pi}\left(\left[H + \frac{2K_2}{M_S}\cos 2\phi - \frac{4K_4}{M_S}\cos 4\phi\right] \times \left[H + 4\pi M_S + \frac{2K_2}{M_S}\cos^2\phi - \frac{K_4}{M_S}(3 + \cos 4\phi)\right]\right)^{1/2}, \quad (2)$$

where K_2 and K_4 are the twofold (uniaxial) and fourfold (cubic) magnetic anisotropy constants, respectively, and ϕ is the angle between H and the easy axis of the sample. The evolution of f is plotted against H, and fitted with the Kittel formula [31] in the presence of both the in-plane and out-of-plane anisotropy constant as given by

$$f = \left(\frac{\gamma}{2\pi}\right)\left[\mu_0 H_X\left(\mu_0 H_X + \mu_0 M_S + \frac{2K_X}{M_S} - \frac{2K_Z}{M_S}\right)\right]^{1/2} \quad (3)$$

for all three samples as shown in Fig. 3(b). The K_x and K_z are the in-plane and out-of-plane anisotropy constants, respectively, and H_X (i.e. H) is the in-plane applied magnetic field. The estimated values of M_S and g from the fitting are 870, 920, and 940 emu/cm^3, and 2.15, 2.15, 2.15 for $B10$, $B20$, and $B30$, respectively. Extracted M_S values agree reasonably well with the values obtained from the vibrating-sample-magnetometer measurement. Figure 3(c) shows the variation in precession frequency as a function of the azimuthal angle φ. Depending on the favorable direction of anisotropy energy, precessional frequency may increase or decrease. In this case, the maximum and minimum frequencies are obtained at the configurations of the $H\|$CFMS [110] direction and the 45° angle in between them, successively, which indicate those directions as magnetic easy axis and hard axis, respectively. We have estimated the values of anisotropy energy by fitting f vs ϕ data using Eq. (2). The values of fourfold anisotropy energy are found out to be -1.37×10^4, -2.36×10^4, and -3.2×10^4 erg/cm^3 for $B10$, $B20$, and $B30$, respectively. In all cases, we find a dominant fourfold magnetocrystalline anisotropy energy due to the cubic symmetry of the structure. Strikingly, the anisotropy energy increases because of regular improvement in cubic crystalline structure with t in agreement with the earlier reports [18,22]. Additionally, a tiny amount of uniaxial anisotropy of 0.70×10^4 erg/cm^3 is also found in $B30$. More importantly, however, we have eliminated the undesirable presence of lattice-mismatch-induced uniaxial anisotropy in the lower thickness regime. To understand the ultrafast demagnetization process in these highly spin-polarized half-metallic samples, we measure the time-resolved Kerr rotation data for the first 5 ps after the zero delay with a temporal resolution of 40 fs for all three CFMS films, as shown in Fig. 4. All of the curves are fitted using an analytical expression [32], as given below,

$$\theta(t) = -\left\{\left[\frac{A_1}{(1 + t/t_0)^{1/2}} - \frac{A_2 t_e - A_1 t_m}{t_e - t_m}e^{-t/t_m} - \frac{t_e(A_1 - A_2)}{t_e - t_m}e^{-t/t_e}\right]H(t) + A_3\delta(t)\right\} \otimes G(t) \quad (4)$$

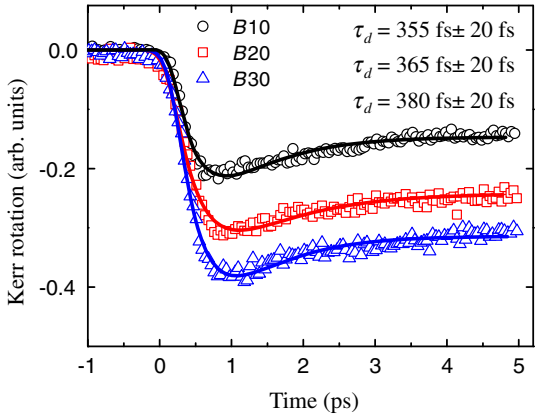

FIG. 4. Ultrafast demagnetization curves for three different samples with different thicknesses. Scattered points are measured data and solid lines are the best fit using Eq. (4). The demagnetization times estimated from fitting are written in the inset.

derived from the rate equations of the three-temperature model. Here, t_m and t_e are the demagnetization time and fast relaxation time, respectively. According to the model the demagnetization time depends on the coupling between the three reservoirs, namely electron, spin, and lattice. In the case of the half-metallic Heusler alloy, this demagnetization process is strongly determined by the spin-scattering process and thus solely related to the spin polarization. The extracted values of demagnetization times are found to be 355 fs ± 20 fs, 365 fs ± 20 fs, and 380 fs ± 20 fs for $B10$, $B20$, and $B30$, respectively. Longer demagnetization times in these samples, in comparison to the 3d ferromagnetic metals, correlate to the high spin polarization as a consequence of suppression of the spin-flip scattering process at around the Fermi level [33,34].

Another interesting part of this study is the variation in the Gilbert damping coefficient in the CFMS thin films with t. Figure 5(a) shows the time-resolved Kerr rotation traces for three different values of t of CFMS thin films. The long-lived uniform precessional Kerr rotation data for all three samples are fitted using a general sine-wave equation superimposed on an exponential decay function in addition to the biexponential background function which is given below

$$M(t) = A + B_1 e^{-t/\tau_{\text{fast}}} + B_2 e^{-t/\tau_{\text{slow}}} + M(0) e^{-t/\tau} \sin(\omega t - \varphi), \quad (5)$$

where τ is the decay time constant and φ is the initial phase of oscillation. τ_{fast} (i.e. t_e) and τ_{slow} are the fast relaxation and slow relaxation time related to the energy transfer between different energy baths (spin, electron, and lattice) subsequently after the ultrafast demagnetization and rate of energy (heat) transfer from the lattice to the surroundings, respectively. The extracted value of the τ_{fast} and τ_{slow} are ~2 and ~550 ps, respectively, from the fitting. The damping

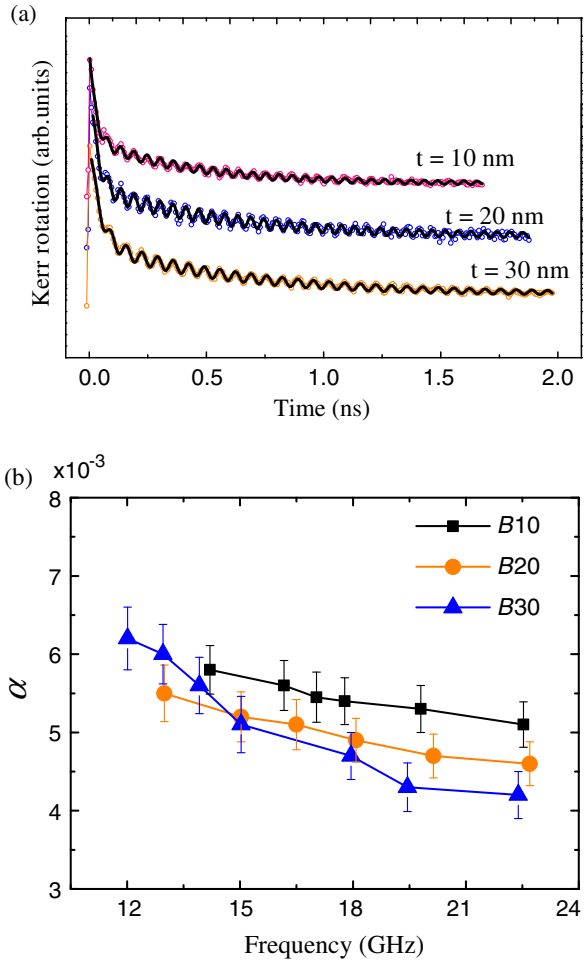

FIG. 5. (a) Time-dependent Kerr rotation data (scattered points) for three different CFMS samples at $H = 1.7$ kOe and their best fits using Eq. (5) (solid lines). (b) Variation in Gilbert damping coefficient (α) as a function of frequency (f).

coefficient (α), which is a combination of both intrinsic and extrinsic contributions, is extracted using the relationship [31] (assuming $K_X = K_Y$ in our case, where K_X and K_Y are the in-plane fourfold anisotropy fields)

$$\alpha = \left[\gamma\tau\mu_0\left(H_X + \frac{K_X}{\mu_0 M_S} - \frac{K_Z}{\mu_0 M_S} + \frac{M_S}{2}\right)\right]^{-1}. \quad (6)$$

The values of K_Z for the three samples are found to be 5×10^5, 5.6×10^5, and 6×10^5 erg/cm^3, respectively. The estimated values of α are plotted as a function of f for all three samples in Fig. 5(b). We achieve a very low value of the damping coefficients of 0.0042 ± 0.0003, 0.0046 ± 0.0003, and 0.0051 ± 0.0003 for $B10$, $B20$, and $B30$, respectively. We have identified two distinct features in the behavior of variation in damping. It is important to note that α decreases very slightly with the precession frequency for $B10$ and $B20$, and saturates at a higher field which is primarily the intrinsic value of α

determined by the inherent spin-orbit coupling strength in CFMS samples. On the contrary, the increment in α with a decreasing frequency becomes more prominent in $B30$ which implies the presence of an extrinsic contribution to the damping phenomenon in addition to the intrinsic part. Earlier reports [35–37] proposed the presence of inhomogeneous anisotropy distribution and two-magnon scattering (TMS) as the extrinsic mechanisms in similar cases. Here, we observe a clear fourfold anisotropy distribution in all three samples with a small amount of uniaxial anisotropy in $B30$. This inhomogeneous anisotropy distribution together with the demagnetizing field in the thicker film can modify the equilibrium field angle, which causes a change in the relaxation time [38]. However, recently our study has shown [18] a frequency-independent value of α even in the presence of both fourfold and uniaxial anisotropy in the same geometry of the external field, ruling out this possible mechanism. Another possible reason is the presence of TMS. Although the TMS effect is primarily known to be a surface effect, it can also occur in the presence of very low-density localized volume impurity in a thicker film where the dynamic magnetization is not so uniform over the volume [39]. The monotonically increasing nature of α towards a peak also indicates the presence of TMS. Hence, we believe the two-magnon scattering due to volume impurity, which is mainly due to the Cr atoms diffused into CFMS, is the primary source of extrinsic damping process.

Interestingly, we obtain a nearly constant very low value of α of about 0.0045 for all three samples at high values of H (>2.3 kOe) where all of the scattering processes get suppressed. In Heusler alloys, the value of α strongly depends on the degree of atomic-site ordering and minority spin density of states [18]. Hence, the stable atomic-site ordering in Cr-buffered CFMS films results in a t-independent low value of α. Here, the t-independent α rules out the possibility of interface spin pumping from the CFMS to the Cr layer. This indicates that the α mainly contains the bulk contribution which is slightly larger in comparison with the CoFeB|MgO case. α is inversely proportional to the saturation magnetization (M_S). Thus, to exclude the effect of M_S, it is worthwhile to calculate the relaxation frequency G ($=\alpha\gamma M_S$). We estimate the values of G to be 73.90 ($t = 30$ nm), 80.07 ($t = 20$ nm), and 83.95 MHz ($t = 10$ nm), which are significantly smaller than the previously reported values of 103.41 [40] and 159 MHz [41] for CoFeB|MgO. Further, it is noteworthy that broadband intrinsic α is achieved for thinner CFMS films. Both the aspects lead to a step ahead for device applications of CFMS in spintronics.

IV. CONCLUSION

In summary, we systematically study the thickness-dependent ultrafast magnetization dynamics in Cr-buffered CFMS thin films, using an all-optical TRMOKE magnetometer. By using Cr as the buffer layer, we are able to achieve a stable Co atomic-site ordering in the $B2$ and $L2_1$ phase. The results show a very low nearly frequency-independent value of the damping coefficient of about 0.0045 in the lower thickness regime, whereas a nonlinear increment in damping with reducing frequency indicates the presence of some extrinsic contribution due to impurity scattering in the higher thickness regime. Despite the increment in both saturation magnetization and anisotropy energy as a function of thickness, surprisingly we obtain a nearly thickness-independent damping coefficient for high strength of the applied magnetic field. Our findings imply the separate origins of anisotropy and damping in the case of CFMS Heusler alloy. Notably, both the thickness and the frequency-independent value of α strongly suggest the suitability of the thinner CFMS film for device application in a broad frequency region.

ACKNOWLEDGMENTS

We acknowledge the financial assistance from the Department of Science and Technology, Government of India, under Grant No. SR/NM/NS-09/2011 and the S. N. Bose National Centre for Basic Sciences under Project No. SNB/AB/12-13/96. This work was partially supported by a Grant-in-Aid for Scientific Research (S) (25220910) from MEXT, Japan and PRESTO "Innovative Nanoelectronics through Interdisciplinary Collaboration among Material, Device and System Layers" (JPMJPR1422). S. P. acknowledges DST, Government of India, for support from INSPIRE Fellowship (IF140999).

[1] J. C. Slonczewski, Current-driven excitation of magnetic multilayers, J. Magn. Magn. Mater. **159**, L1 (1996).
[2] D. C. Ralph and M. D. Stiles, Spin transfer torques, J. Magn. Magn. Mater. **320**, 1190 (2008).
[3] S. Kämmerer, A. Thomas, A. Hütten, and G. Reiss, Co_2MnSi Heusler alloy as magnetic electrodes in magnetic tunnel junctions, Appl. Phys. Lett. **85**, 79 (2004).
[4] R. A. de Groot, F. M. Mueller, P. G. van Engen, and K. H. J. Buschow, New Class of Materials: Half-Metallic Ferromagnets, Phys. Rev. Lett. **50**, 2024 (1983).
[5] I. Galanakis, Ph. Mavropoulos, and P. H. Dederichs, Electronic structure and Slater-Pauling behaviour in half-metallic Heusler alloys calculated from first principles, J. Phys. D **39**, 765 (2006).
[6] I. Galanakis, P. H. Dederichs, and N. Popanikolaou, Slater-Pauling behavior and origin of the half-metallicity of the full-Heusler alloys, Phys. Rev. B **66**, 174429 (2002).
[7] V. Kambersky, On the Landau-Lifshitz relaxation in ferromagnetic metals, Can. J. Phys. **48**, 2906 (1970).
[8] S. Picozzi, A. Continenza, and A. J. Freeman, Co_2MnX (X = Si, Ge, Sn) Heusler compounds: An *ab initio* study of structural, electronic, and magnetic properties at zero and elevated pressure, Phys. Rev. B **66**, 094421 (2002).

[9] M. A. I. Nahid, M. Oogane, H. Naganuma, and Y. Ando, Epitaxial growth of Co_2MnSi thin films at the vicinal surface of *n*-Ge (111) substrate, Appl. Phys. Lett. **96**, 142501 (2010).

[10] F. J. Yang and X. Q. Chen, The microstructure, electronic, and magnetic characterization of highly ordered Co_2MnSi thin films deposited on MgO substrate, Appl. Phys. Lett. **102**, 252407 (2013).

[11] W. H. Wang, M. Przybylski, W. Kuch, L. I. Chelaru, J. Wang, Y. F. Lu, J. Barthel, H. L. Meyerheim, and J. Kirschner, Magnetic properties and spin polarization of Co_2MnSi Heusler alloy thin films epitaxially grown on GaAs (001), Phys. Rev. B **71**, 144416 (2005).

[12] R. Yilgin, Y. Sakuraba, M. Oogane, S. Mizukami, Y. Ando, and T. Miyazaki, Anisotropic intrinsic damping constant of epitaxial Co_2MnSi Heulser alloy films, Jpn. J. Phys. **46**, L205 (2007).

[13] L. Ritchie, G. Xiao, Y. Ji, T. Y. Chen, C. L. Chien, M. Zhang, J. Chen, Z. Liu, G. Wu, and X. X. Zhang, Magnetic, structural, and transport properties of the Heusler alloys Co_2MnSi and NiMnSb, Phys. Rev. B **68**, 104430 (2003).

[14] L. J. Singh, Z. H. Barber, A. Kohn, A. K. Petford-Long, Y. Miyoshi, Y. Bugoslavsky, and L. F. Cohen, Interface effects in highly oriented films of the Heusler alloy Co_2MnSi on GaAs (001), J. Appl. Phys. **99**, 013904 (2006).

[15] B. Balke, G. H. Fecher, H. C. Kandpal, C. Felser, K. Kobayashi, E. Ikenaga, J. J. Kim, and S. Ueda, Properties of the quaternary half-metal-type Heusler alloy $Co_2Mn_{1-x}Fe_xSi$, Phys. Rev. B **74**, 104405 (2006).

[16] A. L. Kwilu, M. Oogane, H. Naganuma, M. Sahashi, and Y. Ando, Intrinsic Gilbert damping constant in epitaxial $Co_2Fe_{0.4}Mn_{0.6}Si$ Heusler alloy films, J. Appl. Phys. **117**, 17D140 (2015).

[17] M. Oogane, T. Kubota, Y. Kota, S. Mizukami, H. Naganuma, A. Sakuma, and Y. Ando, Gilbert magnetic damping constant of epitaxially grown Co-based Heusler alloy thin films, Appl. Phys. Lett. **96**, 252501 (2010).

[18] S. Pan, S. Mondal, T. Seki, K. Takanashi, and A. Barman, Influence of thickness-dependent structural evolution on ultrafast magnetization dynamics in $Co_2Fe_{0.4}Mn_{0.6}Si$ Heusler alloy thin films, Phys. Rev. B **94**, 184417 (2016).

[19] G. Ortiz, A. Garcia-Garcia, N. Biziere, F. Boust, J. F. Bobo, and E. Snoeck, Growth, structural, and magnetic characterization of epitaxial Co_2MnSi films deposited on MgO and Cr seed layers, J. Appl. Phys. **113**, 043921 (2013).

[20] T. Kubota, S. Tsunegi, M. Oogane, S. Mizukami, T. Miyazaki, H. Naganuma, and Y. Ando, Half-metallicity and Gilbert damping constant in $Co_2Fe_xMn_{1-x}Si$ Heusler alloys depending on the film composition, Appl. Phys. Lett. **94**, 122504 (2009).

[21] C. Banerjee, L. M. Loong, S. Srivastava, S. Pal, X. Qiu, H. Yang, and A. Barman, Improvement of chemical ordering and magnetization dynamics Co-Fe-Al-Si Heusler alloy thin films by changing adjacent layers, RSC Adv. **6**, 77811 (2016).

[22] M. S. Gabor, T. Petrisor Jr., C. Tiusan, M. Hehn, and T. Petrisor, Magnetic and structural anisotropies of Co_2FeAl Heusler alloy epitaxial thin films, Phys. Rev. B **84**, 134413 (2011).

[23] Y. Takamura, R. Nakane, and S. Sugahara, Analysis of $L2_1$-ordering in full Heusler Co_2FeSi alloy thin films formed by rapid thermal annealing, J. Appl. Phys. **105**, 07B109 (2009).

[24] W. Wang, H. Sukegawa, R. Shan, T. Furubayashi, and K. Inomata, Preparation and characterization of highly $L2_1$-ordered full Heusler alloy $Co_2Fe_{0.5}Al_{0.5}Si$ thin films for spintronics device applications, Appl. Phys. Lett. **92**, 221912 (2008).

[25] T. Kubota, J. Hamrle, Y. Sakuraba, O. Gaier, M. Oogane, A. Sakuma, B. Hillebrands, K. Takanashi, and Y Ando, Structure, exchange stiffness, and magnetic anisotropy $Co_2MnAl_xSi_{1-x}$ Heusler compounds, J. Appl. Phys. **106**, 113907 (2009).

[26] Y. Miura, K. Nagao, and M. Shirai, Atomic disorder effects on half-metallicity of the full-Heusler alloys $Co_2(Cr_{1-x}Fe_x)Al$: A first-principles study, Phys. Rev. B **69**, 144413 (2004).

[27] M. Oogane, R. Yilgin, M. Shinano, S. Yakata, Y. Sakuraba, Y. Ando, and T. Miyazaki, Structural and dynamic magnetic response of co-sputtered CoFeAl Heusler alloy thin films grown at different substrate temperatures, J. Appl. Phys. **101**, 09J501 (2007).

[28] R. Kelekar, H. Ohldag, and B. M. Clemens, X-ray magnetic circular dichroism of Heusler alloy $Co_2Cr_{1-x}Fe_xAl$ epitaxial thin films, Phys. Rev. B **75**, 014429 (2007).

[29] A. Barman and A. Haldar, *Solid State Physics*, edited by R. E. Camley and R. L. Stamps (Academic Press, Burlington, 2014), Vol. 65, pp. 1–108.

[30] T. Yamamoto, T. Seki, M. Kotsugi, and K Takanashi, Magnetic vortex in epitaxially-grown $Co_2(Fe, Mn)Si$ alloy, Appl. Phys. Lett. **108**, 152402 (2016).

[31] J. Walowski, M. Djordjevic Kaufmann, B. Lenk, C. Hamann, J. McCord, and M. Münzenberg, Intrinsic and non-local Gilbert damping in polycrystalline nickel studied by Ti: sapphire laser fs spectroscopy, J. Phys. D **41**, 164016 (2008).

[32] G. Malinowski, F. Dalla Longa, J. H. H. Rietjens, P. V. Paluskar, R. Huijink, H. J. M. Swagten, and B. Koopmans, Control of speed and efficiency of ultrafast demagnetization by direct transfer of spin angular momentum, Nat. Phys. **4**, 855 (2008).

[33] G. M. Müller, J. Walowski, M. Djordjevic, G.-X. Miao, A. Gupta, A. V. Ramos, K. Gehrke, V. Moshnyaga, K. Samwer, J. Schmalhorst *et al.*, Spin polarization in half-metals probed by femtosecond spin excitation, Nat. Mater. **8**, 56 (2009).

[34] A. Mann, J. Walowski, M. Münzenberg, S. Maat, M. J. Carrey, J. R. Childress, C. Mewes, D. Ebke, V. Drewello, G. Reiss, and A. Thomas, Insights into Ultrafast Demagnetization in Pseudogap Half-Metals, Phys. Rev. X **2**, 041008 (2012).

[35] S. Qiao, S. Nie, J. Zhao, Y. Huo, Y. Wu, and X. Zhang, Magnetic and Gilbert damping properties of $L2_1$-Co_2FeAl film grown by molecular beam epitaxy, Appl. Phys. Lett. **103**, 152402 (2013).

[36] H. C. Yuan, S. H. Nie, T. P. Ma, Z. Zhang, Z. Zheng, Z. H. Chen, Y. Z. Wu, J. H. Zhao, H. B. Zhao, and L. Y. Chen, Different temperature scaling of strain-induced magnetocrystalline anisotropy and Gilbert damping in Co_2FeAl film epitaxied on GaAs, Appl. Phys. Lett. **105**, 072413 (2014).

[37] S. Qiao, S. Nie, J. Zhao, and X. Zhang, The thickness-dependent dynamic magnetic property Co_2FeAl films grown by molecular beam epitaxy, Appl. Phys. Lett. **105**, 172406 (2014).

[38] Ji-Wan Kim, Hyon-Seok Song, Jae-Woo Jeong, Kyeong-Dong Lee, Jeong-Woo Sohn,Toshiyuki Shima, and Sung-Chul Shin, Ultrafast magnetization relaxation in $L1_0$-ordered $Fe_{50}Pt_{50}$ alloy thin film, Appl. Phys. Lett. **98**, 092509 (2011).

[39] P. Krivosik, N. Mo, S. Kalarickal, and C. E. Patton, Hamiltonian formalism for two magnon scattering microwave relaxation: Theory and applications, J. Appl. Phys. **101**, 083901 (2007).

[40] X. Liu, W. Zhang, M. J. Carter, and G. Xiao, Ferromagnetic resonance and damping properties of CoFeB thin film as free layers in MgO-based magnetic tunnel junctions, J. Appl. Phys. **110**, 033910 (2011).

[41] C. Bilzer, T. Devolder, Joo-Von Kim, G. Counil, and C. Chappert, Study of the dynamic magnetic properties of soft CoFeB films, J. Appl. Phys. **100**, 053903 (2006).